HEFAT2010
7th International Conference on Heat Transfer, Fluid Mechanics and Thermodynamics
19-21 July 2010
Antalya, Turkey

IN-FLIGHT ICING SIMULATION WITH SUPERCOOLED LARGE DROPLET EFFECTS

Özgen S.* and Canıbek M.†

*Author for correspondence
Department of Aerospace Engineering,
Middle East Technical University,
Ankara, 06531, Turkey,
E-mail: sozgen@ae.metu.edu.tr

† Flight Sciences Department,
Turkish Aerospace Industries,
Ankara, 06980, Turkey,
E-mail: mcanibek@tai.com.tr

ABSTRACT

In the current study, continued efforts to improve a computational in-flight icing prediction tool are introduced together with the obtained results. The computational method involves flow-field calculation around the wing section using Hess-Smith panel method, droplet trajectory determination and calculation of droplet collection efficiencies using the velocity field thus obtained. Next step is to compute convective heat transfer coefficient distribution over the section using an integral boundary-layer method. Computation of the ice accretion rates by establishing a thermodynamical balance and utilization of the Extended Messinger Method forms the focus of the developed computational tool. Finally, integration of ice accretion rates over time yields the ice shapes and the final geometry. Droplet breakup and droplet splash are accounted for, which are important phenomena for large droplets.

INTRODUCTION

In-flight icing on airframe components is one of the most important problems of civil aviation. Ice formation on the wings, tail surfaces or sensors like pitot tubes seriously threaten flight safety as the aerodynamic performance and control characteristics become seriously and unpredictably degraded.

In order to demonstrate that an airplane can fly safely in icing conditions, certification authorities like FAA and EASA have defined meteorological conditions that the airplane must be tested against in flight tests, laboratory tests and/or computer simulations. However, these conditions are valid for supercooled droplets that have diameters less than 50 microns. There have been incidences and accidents in the past, where the liquid water droplets were much larger, as high as 1000–2000 microns [1]. Therefore a computational simulation tool for ice accretion prediction must be capable of handling a wide range of droplet sizes and associated meteorological conditions.

An overview of the literature related to two-dimensional and three dimensional ice accretion simulations is given by Özgen and Canıbek [2, 3]. Therefore, available literature relating only to large droplet effects will be reviewed here.

The capabilities of LEWICE 1.6 for large drops have been ascertained in [4] by performing a parameter study. A range of drop sizes from 10 to 1000 microns has been selected, local and total collection efficiencies, impingement limits, maximum and total collection efficiencies have been computed for the MS-317 airfoil. Obtained results have been compared to the experimental data coming from the IRT tests.

In [5], a literature search is presented which could be incorporated into icing research. A semi-empirical computational model is presented which incorporates first order physical effects like droplet splash into icing software. Comparisons with supercooled large droplet (SLD) experimental data are made.

Reference [1] describes the validation results obtained by using LEWICE 3.0 and experimental data for collection efficiencies for several airfoils. SLD physics with droplet splash and breakup are introduced and the results are within accuracy limits of the experimental data for most cases.

Reference [6] describes the extensions made to FENSAP-ICE to model mixed-phase flows that combine air, water and ice crystals, and the related ice-accretion. Validation efforts against wind tunnel test results are also presented.

An important reference related to droplet splash physics is a study by Trujillo *et al* [7]. An experimental and computational investigation of spray impingement on a flat surface is presented. A stochastic model for describing droplet properties after splash is developed which includes a splashing criterion, forming the basis for the one utilized in this study.

The current paper describes an original ice-accretion code and the results obtained after including large droplet effects such as droplet breakup and splash. In the following, first, a

brief description of the approach for ice accretion simulation is given, where the methods for flowfield, droplet trajectory, collection efficiency and ice growth rate computations are introduced. Then the code is tested against experimental cases reported in the literature, where large droplet effects are prominent. Obtained results are discussed and interpreted in the same section followed by the conclusions.

NOMENCLATURE

Symbol	*Definition*	*Value and/or unit*
A_p	Droplet cross-sectional area	m^2
B	Ice thickness	m
C_D	Droplet drag coefficient	
C_f	Skin friction coefficient	
C_p	Specific heat of air	1006 J/kg.K
C_{pi}	Specific heat of ice	2050 J/kg.K
C_{pw}	Specific heat of water	4218 J/kg.K
D	Drag force	N
d_p	Droplet diameter	m
d_o	Incident droplet diameter	m
d_s	Splashed droplet diameter	m
g	Gravitational acceleration	9.81 m/s^2
h	Water film height	m
K	Cossali splash parameter	
K_m	Modified Cossali splash parameter	
k_s	Roughness height	m
k	Thermal conductivity of air	0.024 W/m.K*
k_i	Thermal conductivity of ice	2.18 W/m.K
k_w	Thermal conductivity of water	0.571 W/m.K
L_F	Latent heat of solidification	$3.344x10^5$ J/kg
m	Droplet mass	kg
m_o	Incident mass	kg
m_s	Splashed mass	kg
$\dot{m}_{e,s}$	Evaporting or sublimating mass flow rate	kg/m^2s
Oh	Ohnosorge number	
Pr	Laminar Prandtl number of air	0.72
Pr_t	Turbulent Prandtl number of air	0.9
Re	Reynolds number	
St	Stanton number	
T	Temperature (in the ice layer)	K
t_{exp}	Icing exposure duration	s
V_x, V_y	Flow velocity components at the droplet location	m/s
V_∞	Freestream velocity	m/s
V_{rel}	Relative velocity	m/s
$\dot{x}_p, \dot{y}_p$	Droplet velocity components	m/s
$\ddot{x}_p, \ddot{y}_p$	Droplet acceleration components	m/s^2
We	Weber number	
Special Characters		
μ	Kinematic viscosity of ambient air	Pa.s*
μ_w	Viscosity of water	Pa.s*
ν	Dynamic viscosity of air	m^2/s*
ρ	Ambient density	kg/m^3*
ρ_a	Liquid water content	kg/m^3
ρ_r	Density of rime ice	880 kg/m^3
ρ_g	Density of glaze ice	917 kg/m^3
ρ_w	Density of water	999 kg/m^3
σ_w	Surface tension of water	0.072 N/m*
τ	Shear stress	Pa
θ	Temperature in the water layer	K
Subscripts		
i	Ice	
g	Glaze ice	
r	Rime ice	
w	Water	
p	Droplet	
t	Turbulent	

* Temperature dependence is accounted for.

PROBLEM FORMULATION AND SOLUTION METHOD

Flowfield Solution

In order to determine the flow velocities required for droplet trajectory calculations, 2-D Hess-Smith panel method is used [8]. The solution also provides the external velocity distribution around the wing section required for boundary layer calculations yielding the convective heat transfer coefficients.

Droplet Trajectories and Collection Efficiencies

Following assumptions are employed for droplets:

- Droplets are assumed to be spherical,
- The droplets do not affect the flow field,
- Gravity and aerodynamic drag are the only forces acting on the droplets.

Droplet trajectories are computed with the following equations:

$$m\ddot{x}_p = -D\cos\gamma, \tag{1}$$

$$m\ddot{y}_p = -D\cos\gamma + mg, \tag{2}$$

with:

$$\gamma = \tan^{-1}\frac{\dot{y}_p - V_y}{\dot{x}_p - V_x}, \tag{3}$$

$$D = \tfrac{1}{2}\rho\, V_{rel}^2 C_D A_p, \tag{4}$$

$$V_{rel} = \sqrt{(\dot{x}_p - V_x)^2 + (\dot{y}_p - V_y)^2}. \tag{5}$$

Droplet drag coefficients are calculated using the drag law given by Gent *et al* [9]:

$$\begin{aligned} C_D &= 1 + 0.197\,\mathrm{Re}^{0.63} + 2.6\times10^{-4}\,\mathrm{Re}^{1.38}, && \mathrm{Re} \le 3500, \\ C_D &= (1.699\times10^{-5})\,\mathrm{Re}^{1.92}, && \mathrm{Re} > 3500. \end{aligned} \tag{6}$$

In the above formulation, $\mathrm{Re} = \rho V_{rel} d_p/\mu$ is the Reynolds number based on droplet diameter d_p and relative velocity V_{rel}. The viscosity μ is calculated using Sutherland's law as a function of temperature.

Trajectory calculations start from an upstream location far away from the wing section so that air flow velocity components are sufficiently close to their freestream values. The initial droplet velocity is taken to be the terminal velocity:

$$V_{term}^2 = \frac{4}{3}\frac{(\rho_w - \rho)}{\rho}\frac{g d_p}{C_D}. \tag{7}$$

The droplet trajectories are obtained by integrating equations (1) and (2) over time until the droplet impacts the geometry. The droplet impact pattern on the section determines the amount of water that impinges on the surface and the region subject to icing. The local collection efficiency is defined as the ratio, of the area of impingement to the area through which water passes at some distance upstream of the section. The collection efficiency can be defined as $\beta = A_o/A$, where A_o is the area (per unit span) constituted by two adjacent droplets in the release plane, while A is the area of impingement constituted by the same two droplets neighboring a control point.

If the droplet velocity is high enough, the droplet can breakup into smaller droplets due to shear forces acting on its surface. Droplet breaks up when a threshold value of the Weber number, $\mathrm{We} = \rho V_{rel}^2 d_p/\sigma_w$ is exceeded. Although threshold value varies widely in the literature, a value of 12 has been chosen in this study. After breakup, the trajectory calculation is

resumed with the secondary droplet until impact. The secondary particle diameter is obtained from [1]:

$$d_s = 6.2\left(\frac{\rho_w}{\rho}\right)^{0.25} \mathrm{Re}_w^{-0.5}\, d_p \text{ with } \mathrm{Re_w} = \rho_w V_{rel} d_p / \mu_w. \quad (8)$$

After a droplet impacts the surface, part of its mass will impinge on the surface, while the remaining mass will bounce and reimpinge downstream of the initial impact point [10]. The model adopted in this study is to treat the bouncing and reimpinging water as runback water. Cossali *et al* [11] present their results in terms of the non-dimensional group:

$$K = \left(\frac{\rho_w^3 d_p^3 V_n^5}{\sigma_w^2 \mu_w}\right)^{0.25} = \mathrm{Oh}^{-2/5}\mathrm{We_n}. \quad (9)$$

In the above, the Weber number, $\mathrm{We_n}$ is based on the normal component of droplet velocity, V_n at impact. Ohnesorge number is defined as, $\mathrm{Oh} = \mu_w / \sqrt{\rho_w d_p \sigma_w}$. For splash threshold and properties of the splashed droplet a modified version of this parameter is employed: $K_m = \sqrt{K} f^{-3/8}$, where f is a dimensionless droplet frequency defined as follows: $f = (3/2)(\rho_a / \rho_w)^{1/3}$. According to [1], droplet splash occurs when $K_m > 17$ and splashed mass is given by:

$$\frac{m_s}{m_o} = 0.2\left[1 - e^{-0.85(K_m - 17)}\right], \quad (10)$$

where m_o is the incident mass and m_s is the splashed mass. Secondary droplet size is given by [1]:

$$\frac{d_s}{d_p} = 8.72 e^{-0.0281K}. \quad (11)$$

Convective Heat Transfer Coefficients

After flowfield and droplet trajectory calculations, boundary-layer and icing calculations are performed. The current study employs a 2-D Integral Boundary Layer Method for the calculation of the convective heat transfer coefficients. Previous and present results show that the accuracy achieved with this approach is adequate for the purposes of this study.

Transition prediction is based on the roughness Reynolds number, $\mathrm{Re}_k = \rho U_e k_s / \mu$, where k_s is the roughness height and U_e is the external flow velocity at the roughness location.

Roughness height is calculated from [12]:

$$k_s = (4\sigma_w \mu_w / \rho_w F \tau)^{1/3}, \quad (12)$$

where σ_w, ρ_w and μ_w denote the surface tension, density and viscosity of water, respectively. Fraction of the wing section surface that is wetted by water droplets is expressed by F, while τ denotes local surface shear stress.

For laminar flow $(\mathrm{Re}_k < 600)$, formulation of Smith&Spalding is used to calculate the convective heat transfer coefficient [9]:

$$h_c = \frac{0.296 k U_e^{1.435}}{\sqrt{\nu \int_0^s U_e^{1.87} ds}}. \quad (13)$$

where, k is the thermal conductivity of air obtained by assuming constant Prandtl number and viscosity obtained from Sutherland's law as a function of ambient temperature. Streamwise distance along the section starting at the stagnation point is denoted by s. For turbulent flow $(\mathrm{Re}_k \geq 600)$, the method of Kays&Crawford is employed [9]. Accordingly, the turbulent momentum thickness is given by:

$$\theta_t = \frac{0.036\nu^{0.2}}{U_e^{3.29}}\left(\int_{s_{tr}}^{s} U_e^{3.86} ds\right)^{0.8} + \theta_{tr}, \quad (14)$$

where s_{tr} is the onset of transition location and θ_{tr} is the corresponding laminar momentum thickness. Skin friction coefficient is computed from the Makkonen relation [9]:

$$\frac{C_f}{2} = \frac{0.1681}{\left[\ln(864\theta_t / k_s + 2.568)\right]^2}. \quad (15)$$

The Stanton number can be calculated from:

$$\mathrm{St} = \frac{C_f / 2}{\mathrm{Pr_t} + \sqrt{(C_f/2)/\mathrm{St_k}}}, \quad (16)$$

where $Pr_t = 0.9$ is the turbulent Prandtl number. The roughness Stanton number is given as:

$$\mathrm{St_k} = 1.92\,\mathrm{Re_k}^{-0.45}\,\mathrm{Pr}^{-0.8}, \quad (17)$$

where $\mathrm{Pr} = \mu C_p / k = 0.72$ is the laminar Prandtl number. The turbulent convective heat transfer coefficient is evaluated from:

$$h_c = \mathrm{St}\rho U_e C_p, \quad (18)$$

Extended Messinger Method

The ice prediction approach employed in this study is introduced in detail by Özgen and Canıbek [2]. The ice shape prediction is based on the method of phase change. The problem is governed by four equations: two energy equations in the ice and water layers, mass conservation equation and a phase change condition at the ice/water interface [13]:

$$\frac{\partial T}{\partial t} = \frac{k_i}{\rho_i C_{pi}} \frac{\partial^2 T}{\partial y^2}, \quad (19)$$

$$\frac{\partial \theta}{\partial t} = \frac{k_w}{\rho_w C_{pw}} \frac{\partial^2 \theta}{\partial y^2}, \quad (20)$$

$$\rho_i \frac{\partial B}{\partial t} + \rho_w \frac{\partial h}{\partial t} = \rho_a \beta V_\infty + \dot{m}_{in} - \dot{m}_{e,s}, \quad (21)$$

$$\rho_i L_F \frac{\partial B}{\partial t} = k_i \frac{\partial T}{\partial y} - k_w \frac{\partial \theta}{\partial y}, \quad (22)$$

where θ and T are the temperatures, k_w and k_i are the thermal conductivities, C_{pw} and C_{pi} are the specific heats and h and B are the thicknesses of water and ice layers, respectively. In equation (21), $\rho_a \beta V_\infty$, $\dot{m}_{in}$ and $\dot{m}_{e,s}$ are impinging, runback and evaporating (or sublimating) water mass flow rates for a control volume (panel), respectively. In equation (22), ρ_i and L_F denote the density of ice and the latent heat of solidification of water, respectively. Ice density is assumed to have two different values for rime ice (ρ_r) and glaze ice (ρ_g), see Nomenclature. The coordinate y is normal to the surface. In order to determine the ice, water thicknesses and the temperature distribution at each layer, boundary and initial conditions must be specified. These are based on the following assumptions [13]:

i. Ice is in perfect contact with the profile surface, taken to be equal to the adiabatic wall temperature, T_{ad}:

$$T(0,t) = T_s = T_{ad}. \quad (23)$$

ii. The temperature is continuous at the ice/water boundary and is equal to the freezing temperature:

$$T(B,t) = \theta(B,t) = T_f. \quad (24)$$

iii. At air/water (glaze ice) or air/ice (rime ice) interfaces, heat flux is governed by convection (Q_c), radiation (Q_r), latent heat release (Q_l), cooling by incoming droplets (Q_d), heat brought by runback water (Q_{in}), evaporation (Q_e) or sublimation (Q_s), aerodynamic heating (Q_a) and kinetic energy of incoming droplets (Q_k):

Glaze ice:

$$-k_w \frac{\partial \theta}{\partial y} = (Q_c + Q_e + Q_d + Q_r) - (Q_a + Q_k + Q_{in}) \quad \text{at} \quad y = B + h. \quad (25)$$

Rime ice:

$$-k_i \frac{\partial T}{\partial y} = (Q_c + Q_s + Q_d + Q_r) - (Q_a + Q_k + Q_{in} + Q_l) \quad \text{at} \quad y = B. \quad (26)$$

iv. Wing surface is initially clean:

$$B = h = 0, \quad t = 0. \quad (27)$$

For the definitions of the heat terms in equations (25) and (26), see Özgen and Canıbek [2].

Rime Ice Growth and Temperature Distribution:

In the current approach, each panel constituting the geometry is also a control volume. The above equations are written for each panel and ice is assumed to accumulate perpendicularly to a panel. This is an extension of the one-dimensional model described by Myers [13] to two-dimensional, which is done by taking mass and energy terms due to runback water flow in the conservation equations into account as it is done in equation (21).

Rime ice thickness can be obtained directly from the mass conservation equation (21) as water droplets freeze immediately on impact:

$$B(t) = \frac{\rho_a \beta V_\infty + \dot{m}_{in} - \dot{m}_s}{\rho_r} t. \quad (28)$$

It has been shown that, for ice thicknesses less than 2.4 cm (which the case for most applications), the temperature distribution is governed by the following equation [13]:

$$\frac{\partial^2 T}{\partial y^2} = 0. \quad (29)$$

Integrating the above equation twice and applying the boundary and interface conditions given in equations (23) and (26) results in the following temperature distribution in the rime ice layer:

$$T(y) = T_s + \frac{(Q_a + Q_k + Q_{in} + Q_l) - (Q_c + Q_d + Q_s + Q_r)}{k_i} y. \quad (30)$$

Glaze Ice Growth and Temperature Distribution:

It has been shown that, if ice and water layer thicknesses are less than 2.4 cm and 3 mm respectively (true for most applications), the temperature distributions in the ice and water layers are governed by the following equations [13]:

$$\frac{\partial^2 T}{\partial y^2} = 0, \quad \frac{\partial^2 \theta}{\partial y^2} = 0. \quad (31)$$

After integrating above equation twice and employing the conditions (23) and (24), the temperature distribution in the ice:

$$T(y) = \frac{T_f - T_s}{B} y + T_s. \quad (32)$$

The temperature distribution in the water layer is obtained by integrating equation (31) twice and employing the interface conditions (24) and (25):

$$\theta(y) = T_f + \frac{(Q_a + Q_k + Q_{in}) - (Q_c + Q_d + Q_e + Q_r)}{k_w} (y - B). \quad (33)$$

Integrating mass conservation equation (21) yields the water height, h:

$$h = \frac{\rho_a \beta V_\infty + \dot{m}_{in} - \dot{m}_e}{\rho_w} (t - t_g) - \frac{\rho_g}{\rho_w} (B - B_g), \quad (34)$$

where B_g is the rime ice thickness at which glaze ice first appears and t_g is the time at which this happens. When equation (34) is substituted into the phase change condition in equation (22), a first order ordinary differential equation for the ice thickness is obtained:

$$\rho_g L_F \frac{\partial B}{\partial t} = \frac{k_i (T_f - T_s)}{B} + k_w \frac{(Q_c + Q_e + Q_d + Q_r) - (Q_a + Q_k + Q_{in})}{k_w}. \quad (35)$$

During transition from rime ice to glaze ice, ice growth rate must be continuous:

$$\left(\frac{\partial B}{\partial t}\right)_{rime} = \left(\frac{\partial B}{\partial t}\right)_{glaze} \quad \text{at } B=B_g \text{ or } t=t_g. \quad (36)$$

Using equations (28) and (35) yields:

$$B_g = \frac{k_i (T_f - T_s)}{(\rho_a \beta V_\infty + \dot{m}_{in} - \dot{m}_{sub}) L_F + (Q_a + Q_k + Q_{in}) - (Q_c + Q_d + Q_e + Q_r)}, \quad (37)$$

$$t_g = \frac{\rho_r}{\rho_a \beta V_\infty + \dot{m}_{in} - \dot{m}_s} B_g. \quad (38)$$

In order to calculate the glaze ice thickness as a function of time, equation (35) is integrated numerically over time for the duration of the icing exposure, t_{exp} using a Runge-Kutta-Fehlberg method.

RESULTS AND DISCUSSION

Droplet Splash Effects

In Figures 1 and 2, the collection efficiency results are compared with experimental data reported in [5] for d_p=21μm, α=0° and α=8°, respectively. The airfoil is MS-317 with a chord length of 0.915m, the liquid water content is 0.5 g/m^3 and the freestream velocity is 78 m/s. It can be seen that including splash and breakup effects significantly reduces the maximum collection efficiency. For these conditions, including these effects worsens the collection efficiency predictions.

In Figures 3 and 4, results are presented for d_p=92μm, all other conditions being same as in Figures 1 and 2. Again, inclusion of splash and breakup effects significantly reduces the maximum and overall collection efficiency levels, providing a better rendering of experimental results. The agreement is better for the suction side of the airfoil. Although the maximum collection efficiency levels of the experimental data is well captured, there is still room for improvement for the collision limit predictions and overall collection efficiency levels.

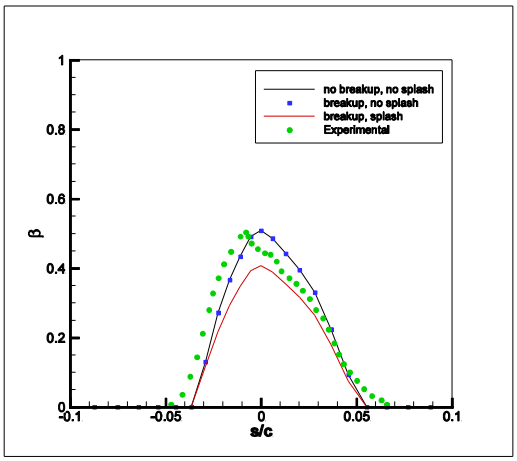

Figure 1 Collection efficiency for d_p=21μm, α=0°.

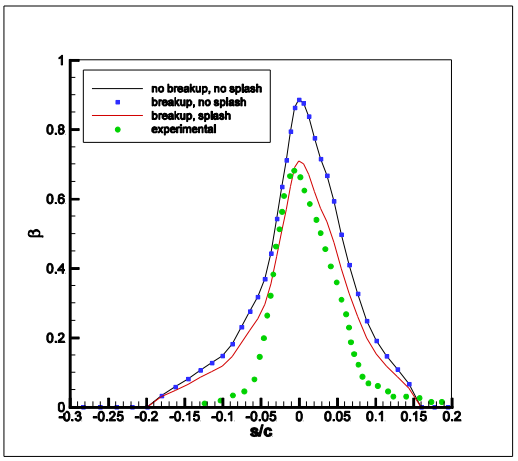

Figure 3 Collection efficiency for d_p=92μm, α=0°.

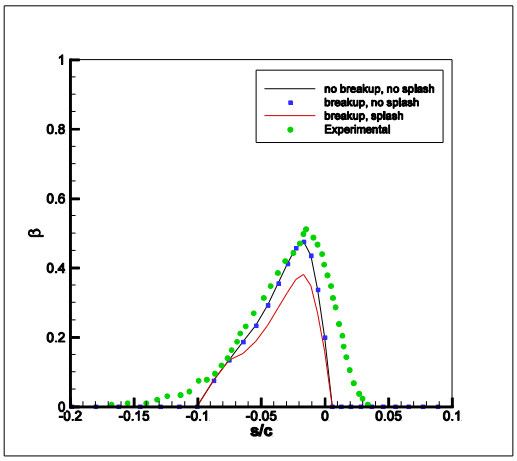

Figure 2 Collection efficiency for d_p=21μm, α=8°.

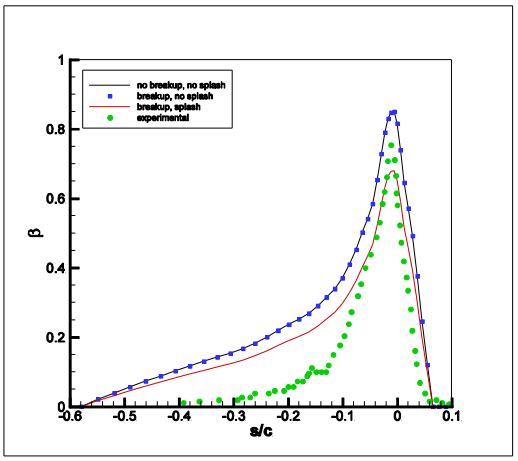

Figure 4 Collection efficiency for d_p=92μm, α=8°.

Figures 5 and 6 compare the current results with numerical results reported in [5] for d_p=236μm. The conditions are otherwise the same as for Figures 1-4. There is no experimental data reported for these cases, however. These figures present an important finding. The results of the Trujillo model reported in [5] are very close to those obtained in the current study, suggesting that the droplet trajectory computation method used in the current study is correct, and the disagreement of the current results with experimental data is probably due to the splash model used. Although the current splash model improves the results, further improvement could still be made by using more sophisticated splash models like those mentioned in [1].

For the range of conditions studied in Figures 1-6, the droplet breakup model seems to have almost no effect, a point that is further elaborated below.

Droplet Breakup Effects

In Figure 7, the effect of droplet breakup is shown (droplet splash feature is switched off). It seems that droplet breakup has an effect for large droplets and only when the freestream velocity is sufficiently high. The calculations have been repeated for lower velocities and at the same droplet diameter, yielding much less significant results than the ones presented. This inference is in agreement with that reported in [5].

Ice Shape Predictions

In Figures 8 and 9, ice shape predictions of the current tool are compared to experimental results reported in [5]. The airfoil is NACA 0012 with a chord length of 0.53m and angle of attack is 0°. The experimental conditions are given in Table 1.

Table 1 Experimental conditions for Figures 8 and 9.

	d_p (μm)	ρ_a (g/m^3)	V_∞ (m/s)	T_∞ (°C)	t_{exp} (s)
Figure 8	160	1.5	52	-19.5	300
Figure 9	160	1.04	77	-19.2	336

From Figure 8, it can be seen that inclusion of droplet splash and breakup features in the developed tool does not significantly improve the agreement of the obtained results with the experimental ones for this parameter combination. Nevertheless, the agreement is acceptable.

However, in Figure 9, inclusion of splash and breakup effects significantly improve the predictions of the current tool. The flow velocity is higher in this case, which seems to increase the effect of splashing phenomena.

CONCLUSIONS

The improvements related to large droplet effects made on an original ice prediction tool is presented together with obtained results. Results indicate that droplet splash can constitute a significant effect especially when the flow velocity

and droplet sizes are sufficiently large. On the other hand, droplet breakup seems to have a secondary effect compared to droplet splash but is included in the developed tool, since its inclusion does not require significant computational effort and does not penalize cpu and storage requirements.

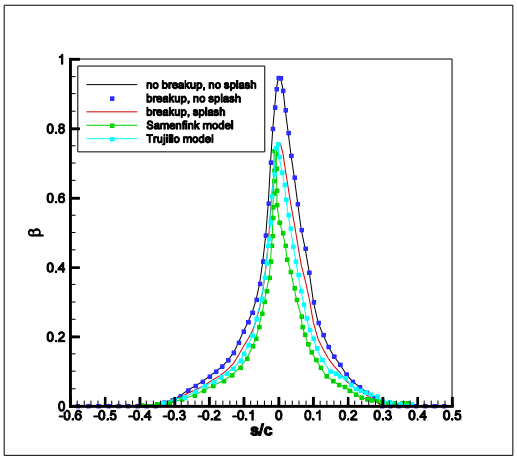

Figure 5 Collection efficiency for d_p=236μm, α=0°.

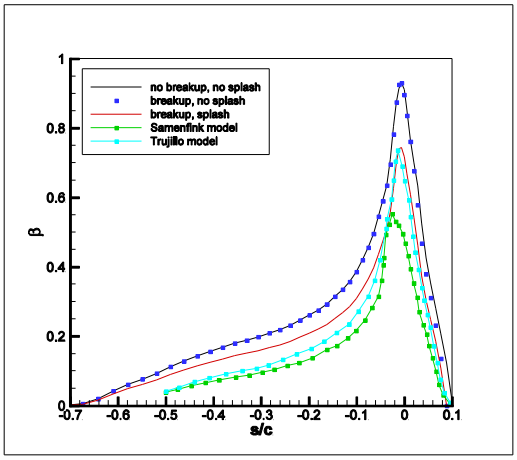

Figure 6 Collection efficiency for d_p=236μm, α=8°.

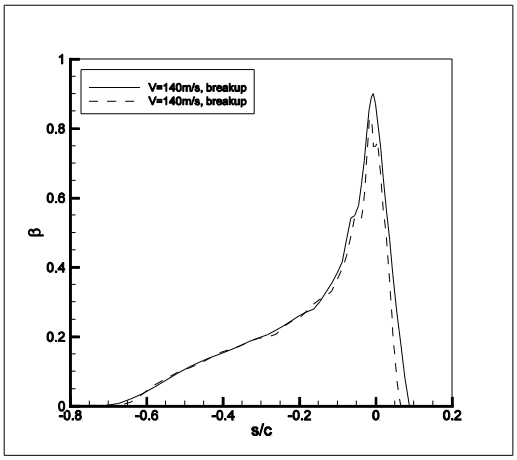

Figure 7 Collection efficiency for d_p=236μm, α=8°.

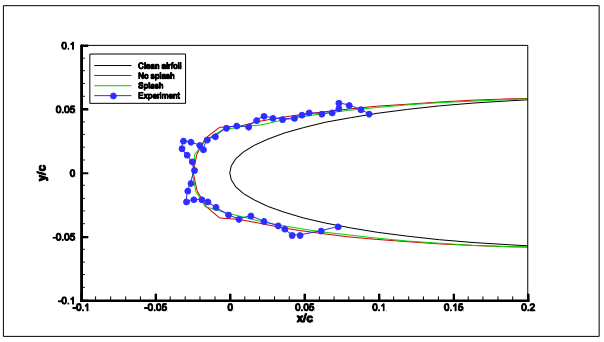

Figure 8 Ice shape comparison, V_∞=52 m/s.

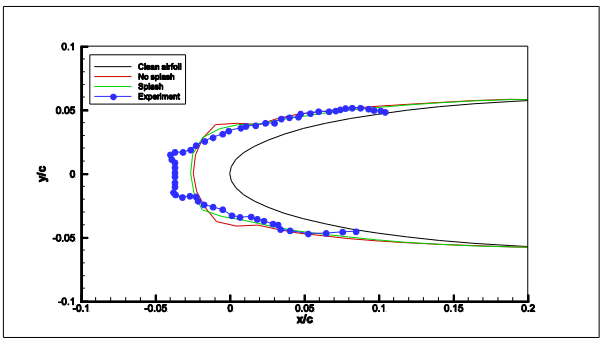

Figure 9 Ice shape comparison, V_∞=77 m/s.

REFERENCES

[1] Wright, W.B., Validation Results for LEWICE 3.0, NASA/CR-2005-213561, 2005.

[2] Özgen, S., and Canıbek, M., Ice Accretion Simulation on Multi-Element Airfoils using Extended Messinger Model, *Heat and Mass Transfer*, Vol. 45, 2009.

[3] Özgen, S., and Canıbek, M., In-Flight Ice Formation Simulation on Finite Wings and Air Intakes, *Heat and Mass Transfer*, 2010 (in review).

[4] Wright, W.B. Capabilities of LEWICE 1.6 and Comparison with Experimental Data, *presented at the AHS Icing Symposium, Montreal, Canada,* 1995.

[5] Wright, W.B., and Potapczuk, M.G., Semi-Empirical Modeling of SLD Physics, NASA/TM-2004-212916, 2004.

[6] Nilamdeen, S., Habashi, W.G., Aube, M.S., and Baruzzi, G.S., FENSAP-ICE: Modeling of Water Droplets and Ice Crystals, *proceedings of the 1st AIAA Atmospheric and Space Environments Conference, San Antonio, Texas, USA*, 2009.

[7] Trujillo, M.F., Mathews, W.S., Lee, C.F., and Peters, J.E., Modelling and Experiment of Impingement and Atomization of a Liquid Spray on a Wall, *Int. J. Eng. Research,* Vol. 1, 2000.

[8] Katz, J., and Plotkin, A., *Low Speed Aerodynamics,* Springer-Verlag, Berlin and New York, 1984.

[9] Gent, R.W., Dart, N.P., and Cansdale, J.T., Aircraft Icing, *Phil. Trans. R. Soc. Lond. A*, Vol. 358, 2000.

[10] Wright, W.B., and Potapczuk, M. G., Computational Simulation of Large Droplet Icing, *Proceedings of the FAA International Conference on Aircraft Inflight Icing*, 1996.

[11] Cossali, G.E., Coghe, A., and Marengo, M., The impact of a single drop on a wetted solid surface, *Exp. Fluids,* Vol. 22, 1997.

[12] Wright, W., Gent, R., and Guffond, D., DRA/NASA/ONERA Collaboration on Icing Research, Part II, Prediction of Airfoil Ice Accretion, NASA CR_202349, 1997.

[13] Myers, T.G., Extension to the Messinger Model for Aircraft Icing, *AIAA J.*, Vol. 39, 2001.